GEOPHYSICS, VOL. 82, NO. 6 (NOVEMBER-DECEMBER 2017); P. WB47–WB61, 13 FIGS.
10.1190/GEO2016-0625.1

SWIP: An integrated workflow for surface-wave dispersion inversion and profiling

Sylvain Pasquet[1] and Ludovic Bodet[2]

ABSTRACT

The simultaneous estimation of 2D pressure (P-) and S-wave velocities (V_P and V_S, respectively) is a promising approach for imaging subsurface mechanical properties. It can be performed with a single acquisition setup by combining P-wave refraction and surface-wave (SW) analysis. Although SW methods are commonly applied for the 1D estimation of V_S, 2D profiling requires the implementation of specific processing and inversion tools not yet widely available in the community. We have developed an open-source MATLAB-based package that performs SW inversion and profiling (SWIP) so as to retrieve 1D to 2D variations of V_S from any kind of linear active-source near-surface seismic data. Each step of the workflow involves up-to-date processing and inversion techniques and provides ready-to-use outputs with quality control tools. First, windowing and stacking techniques are implemented to enhance the signal-to-noise ratio and extract local dispersion images along the line. Then, dispersion curves are picked for each window with an uncertainty range in the phase velocity including higher uncertainties at low frequency. These curves are next inverted using a Monte Carlo approach with various parameterizations (e.g., user defined, refraction based). The best models are finally selected according to their fit to the data to build an average final model with a suggested investigation depth. As an example, we used SWIP to process data collected at a Yellowstone hydrothermal system. Our results show the benefits of estimating V_P and V_S from a single seismic setup to highlight subsurface gas pathways.

INTRODUCTION

Seismic methods are classically used for near-surface applications (in general, at depths shallower than 100 m) to determine the main mechanical properties of the subsurface. More particularly, the joint estimation of pressure (P-) and S-wave velocities (V_P and V_S, respectively) is often proposed for engineering purposes, such as landslide characterization (Godio et al., 2006; Jongmans et al., 2009; Socco et al., 2010b; Hibert et al., 2012; Uhlemann et al., 2016), fill compaction control (Uyanık, 2011; Cardarelli et al., 2014), or earthquake site response assessment (Jongmans, 1992; Lai and Rix, 1998; Raptakis et al., 2000; Othman, 2005). More recently, the combined use of V_P and V_S has been applied to critical zone science, with an increasing interest in the Poisson's ratio derived from those velocities. For example, this approach has been used to study subsurface weathering processes (Olona et al., 2010), image hydrothermal fluid pathways (Pasquet et al., 2016b), characterize aquifer systems (Turesson, 2007; Grelle and Guadagno, 2009; Mota and Monteiro Santos, 2010; Konstantaki et al., 2013; Pasquet et al., 2015a, 2015b), and perform time-lapse monitoring of shallow water content (Bergamo et al., 2016a, 2016b; Dangeard et al., 2016; Pasquet et al., 2016a).

For these near-surface studies, V_P is typically retrieved with P-wave refraction tomography using a flat plate and hammer source with vertical component geophones (Parsekian et al., 2015). The use of this method is widespread because it is easily implemented with a 1D to 3D coverage, quick to set up, and relatively inexpensive. When applied for the estimation of V_S (e.g., Pasquet et al., 2015b), seismic refraction is mostly carried out using specific sources strenuous to handle (Jongmans and Demanet, 1993; Sheriff and Geldart, 1995; Xia et al., 2002; Haines, 2007) and horizontal component geophones difficult to install horizontally (Sambuelli

Peer-reviewed code related to this article can be found at http://software.seg.org/2017/0008.
Manuscript received by the Editor 1 December 2016; revised manuscript received 19 May 2017; published ahead of production 21 July 2017; published online 06 September 2017.
[1]Formerly University of Wyoming, Department of Geology and Geophysics, Laramie, Wyoming, USA; presently Virginia Polytechnic Institute and State University, Department of Geosciences, Blacksburg, Virginia, USA. E-mail: spasquet@vt.edu.
[2]Sorbonne Universités, Paris, France. E-mail: ludovic.bodet@upmc.fr.

et al., 2001). More recently, S-wave-dominated wavefields have also been recorded using either multicomponent geophones with vectorial seismic sources (Schmelzbach et al., 2016) or vertical single-component geophones with source- and receiver-side gradients (Sollberger et al., 2016). Although these approaches appear promising, they usually require a supplementary acquisition or specific equipment with limited availability among practitioners. As an alternative, surface-wave (SW) seismic methods are commonly proposed to infer the 1D V_S structure of earth and subsurface materials (e.g., Gabriels et al., 1987; Jongmans and Demanet, 1993; Park et al., 1999; Rix et al., 2001; O'Neill et al., 2003; Socco and Strobbia, 2004; Socco et al., 2010a; Bergamo and Socco, 2016). When these methods are used to characterize near-surface 2D variations of V_S, they are mainly implemented along linear sections using active-source prospecting in roll-along mode. SW data are basically extracted and inverted from typical seismic shot gathers, providing a collection of 1D V_S profiles merged to obtain a pseudo-2D V_S section (Socco and Strobbia, 2004; Socco et al., 2010a).

Although numerous techniques have been proposed to process and invert SW data over the past 15 years, only a few of them have been made available to the practitioners' community, especially when it comes to 2D profiling. To address this shortcoming, we present here a free and open-source MATLAB-based software package that performs SW dispersion inversion and profiling (SWIP) (Pasquet, 2017). SWIP makes it possible to retrieve 1D to 2D variations of V_S from any kind of active-source near-surface seismic data recorded along linear profiles. It is particularly adapted (but not limited) to process seismic data originally collected to estimate V_P from P-wave refraction tomography. In that case, it allows one to extract supplementary V_S information from already acquired data sets, thus improving the understanding of subsurface structures and processes. Each step of the implemented workflow involves up-to-date processing and inversion techniques, mostly available in the literature. These different steps are integrated within five MATLAB modules, each one automatically calling the necessary functions and softwares. Specifically, seismic data are handled with the open-source software package Seismic Unix (SU), whereas the inversion is performed using the open-source software package Geopsy. In the following, we first give a short review of the existing strategies and methods used for SW profiling. We then present the selected approach with a detailed description of each processing step, including the corresponding theoretical background, technical elements, and associated notations. We finally use field data collected at a shallow hydrothermal system in Yellowstone National Park (USA) to illustrate how SWIP provides ready-to-use outputs with extensive quality control tools.

BACKGROUND METHODOLOGY: FROM 1D TO 2D

Surface waves are, basically, guided along the earth's surface with their amplitude decreasing exponentially with depth. Most of their energy is thus confined in the shallow subsurface where mechanical properties usually vary significantly with depth. SW propagation velocities are therefore different for high frequencies (short wavelengths) confined in the shallow subsurface than for low frequencies, which are influenced by deeper materials. In addition, these velocities are strongly linked to the shear properties of the material through which SWs propagate. The aforementioned velocity dependence on frequency, commonly referred to as dispersion, is then related to V_S of the medium. Because SWs are of higher amplitudes than body waves, this dispersion can be quite easily extracted from typical shot gathers using a wavefield transform. The shot gathers, originally recorded in the distance-time domain, are transformed into the frequency-wavenumber (or frequency-phase velocity) domain, in which maxima should correspond to SW propagation modes (McMechan and Yedlin, 1981; Russel, 1987; Mokhtar et al., 1988; Sheriff and Geldart, 1995; Strobbia and Foti, 2006). Because 1D forward-modeling techniques of SW dispersion are well-established, straightforward, and of low computational cost, it is possible to invert these data for a 1D V_S structure along the seismic spread (see, for instance, reviews of Socco and Strobbia [2004] and Socco et al. [2010a] for more details about the theoretical and methodological aspects as well as classic literature about the topic).

In the early 2000s, SW methods have rapidly grown in popularity among near-surface practitioners with their access to multichannel equipment and the development of dedicated techniques and the associated software. Among those techniques, multichannel analysis of surface waves (Miller et al., 1999; Park et al., 1999; Xia et al., 1999) pioneered 2D profiling by repeating identical single-shot seismic acquisitions along a profile, then extracting dispersion curves from each of these acquisitions. When targeting 2D shallow structures with strong lateral variability, this method is, however, limited by the assumption that the probed medium is horizontally layered below each acquisition setup, as imposed by its 1D inverse problem formulation (Sambridge and Mosegaard, 2002). In the presence of strong lateral variations, the dispersion image obtained from a classical seismic setup corresponds to a 1D equivalent medium that cannot be used to infer 2D characteristics of the true medium (Bodet et al., 2005). Although these images could be interpreted in two dimensions using full-waveform seismic modeling (e.g., Martin and Komatitsch, 2009; Dhemaied et al., 2011), the computational cost of such an approach has led scientists to look for more practical and time-efficient solutions.

Taking advantage of redundant seismic data, several techniques have been developed to overcome these limitations. For example, O'Neill et al. (2003) propose a more comprehensive strategy providing local dispersion images along a profile, using a fixed acquisition setup and several sources interspersed between the geophones. The procedure consists of computing dispersion images from identical subsets of the seismic setup illuminated by different shots, then stacking the dispersion images obtained for each subset to increase the signal-to-noise ratio (S/N) and enhance the identification of SW propagation modes. In the meantime, Hayashi and Suzuki (2004) propose an approach based on the analysis of common midpoint crosscorrelations (CMPCC). With this technique, crosscorrelations are initially calculated for each shot between all pairs of traces. Then, those having identical common midpoints (CMPs) are combined and sorted by the distance between each pair of traces, resulting in a shot gather from which a local dispersion image associated with the CMP position can be extracted. Those two main approaches have subsequently been adapted and applied to numerous geophysical problems. For instance, Bohlen et al. (2004) use a Gaussian moving window to extract the dispersion of Scholte waves from marine seismic data, whereas Grandjean and Bitri (2006) combine the stacking tools proposed by O'Neill et al. (2003) to the crosscorrelation technique developed by Hayashi and Suzuki (2004) to increase the S/N of local CMPCC dispersion images. Soon after, Neducza (2007) proposes a generalization of the stacking and windowing techniques described by O'Neill et al. (2003), introducing systematic parameters controlling the extraction of dispersion images along a seismic profile. More recently, Boiero and Socco (2011) and Bergamo et al. (2012) propose using a series of Gaussian moving windows to extract local dispersion images from a single seismic setup with a limited number of sources located on either side of the spread, following the work of Socco et al. (2009) and Boiero and Socco (2010). A similar windowing technique is also used by Ikeda et al. (2013) to improve the lateral resolution of the CMPCC method.

Once extracted from the dispersion images, dispersion curves are generally inverted to estimate a 1D V_S model below the extraction spread. Forward analytical and semianalytical modeling techniques, such as the Thomson-Haskell matrix propagator (Thomson, 1950; Haskell, 1953) or the reflection-transmission coefficients (Kennett, 1974), enable rapid calculation of modal solutions of the SW dispersion relation in a 1D medium and are commonly used for SW applications. These forward models are implemented in various inversion schemes, the most common being damped or constrained least-squares techniques (Lai et al., 2002; O'Neill et al., 2003; Herrmann, 2013). From a practical point of view, these local optimization methods have a relatively low computational cost, which, for instance, facilitates the implementation of laterally constrained inversion schemes applied to the 2D characterization of the medium (Socco et al., 2009). Alternatively, global optimization methods have been increasingly proposed to widely investigate the parameter space and provide a more comprehensive solution (Socco and Boiero, 2008; Wathelet, 2008). Several of these methods have been applied to SW inversion, including genetic algorithms (Lomax and Snieder, 1994; Nagai et al., 2005; Song et al., 2012, 2015), simulated annealing (Martínez et al., 2000; Beaty et al., 2002), or the neighborhood algorithm (NA) (Sambridge, 1999a; Wathelet et al., 2004).

IMPLEMENTED WORKFLOW AND BACKGROUND THEORY

As stated above, SWIP is mainly designed to retrieve 1D to 2D variations of V_S from typical near-surface seismic data collected along linear profiles with various acquisition geometries (e.g., off-end shots, successive roll along). It is particularly adapted (but not limited) to process data sets that were originally designed to estimate V_P from P-wave refraction tomography and thus extract supplementary V_S information. Each step of the designed workflow is described as follows:

1) We implemented windowing techniques adapted from O'Neill et al. (2003) and Neducza (2007) to narrow down the lateral extent of the dispersion measurements and realistically consider a 1D medium below each extraction spread, thus achieving the required lateral resolution for 2D profiling.
2) Seismic data are then transformed in the frequency-phase velocity domain, in which phase velocities can clearly be identified. For this step, we implemented a slant stack in the frequency domain, as described by Russel (1987) and Mokhtar et al. (1988).
3) To compensate the loss of spectral resolution caused by windowing the data (Gabriels et al., 1987), we implemented stacking techniques, also adapted from O'Neill et al. (2003) and Neducza (2007), to enhance S/N, limit near-field effects, and give access to larger wavelengths necessary for increasing investigation depth (Russel, 1987; Forbriger, 2003a, 2003b; O'Neill, 2003; Bodet et al., 2005, 2009; O'Neill and Matsuoka, 2005; Zywicki and Rix, 2005).
4) Dispersion curves are extracted for each window with phase-velocity uncertainty taking into account resolution limitations at low frequency, following the algorithm described by O'Neill (2003).
5) These curves are then inverted for each window position using the NA (Sambridge, 1999a; Wathelet et al., 2004) with different possible parameterizations (e.g., user-defined, refraction based).
6) Models matching the observed data within the uncertainty range (Endrun et al., 2008) are selected to build a mean average or misfit-weighted final model and estimate the investigation depth through their standard deviation or from empirical criteria.
7) One-dimensional V_S models obtained for each extraction window are ultimately merged into a pseudo-2D section of V_S (Pasquet et al., 2015b).

As stated above, these processing and inversion steps consist mostly in up-to-date techniques available in the literature. However, SWIP users can easily suggest (and implement) alternative approaches if more appropriate methods are required and/or more specific applications are targeted. A detailed description of each step is given, including the corresponding theoretical background, technical elements, and associated notations.

Extraction of dispersion

SWIP takes advantage of multishot acquisition setups to retrieve the lateral variations of SW (i.e., Rayleigh or Love depending on the source and geophone component) dispersion using shot gather windowing and dispersion stacking. Data handling is achieved using the open-source software package SU (Stockwell, 2017) after converting standard SEG2 or ASCII data into the SU format. Although the wavefield transform is performed after data windowing in the actual workflow, it is presented first in the following to introduce resolution issues that are critical to understand the relevance of data windowing and dispersion stacking. The dispersion extraction procedure is illustrated by the flowchart in Figure 1.

Wavefield transform (module A)

Seismic data are generally recorded in the distance-time domain, in which the contribution of SWs ($S(x,t)$) can be described as the superposition of an infinite number of propagation modes (Aki and Richards, 1980; Russel, 1987):

$$S(x,t) = \frac{1}{2\pi}\int_{-\infty}^{+\infty}\sum_m A_m(\omega,x)e^{i(\omega t - k_m(\omega)x)}d\omega, \quad (1)$$

where ω is the frequency, $A_m(\omega,x)$ is the amplitude spectrum of the seismic signal, and $k_m(\omega)$ is the wavenumber for the propagation mode m. Phase velocity c and slowness p are defined for each mode m as

$$c_m(\omega) = \frac{1}{p_m(\omega)}, \quad (2)$$

$$= \frac{\omega}{k_m(\omega)}. \quad (3)$$

Although these velocities are difficult to estimate in the distance-time domain, they can be clearly identified in the frequency-phase velocity domain. It is therefore necessary to transform the wavefield from one domain to another. For this purpose, we implemented a slant stack in the frequency domain (p-ω stack) as defined by Russel (1987) and Mokhtar et al. (1988). The p-ω stack of a multimode SW can be written as

$$U(\omega, p) = \sum_{n=1}^{N} \frac{A(\omega, x_n)e^{i(\phi_n+\omega p x_n)}}{A(\omega, x_1)e^{i\phi_1}}, \tag{4}$$

where $A(\omega, x_n)$ is the amplitude spectrum of the nth trace ($n = 1, 2, \ldots, N_x$) at a distance x_n and ϕ_n is its phase spectrum. Before this operation, the data are multiplied by the square root of the distance to correct for geometric spreading, as recommended by Gabriels et al. (1987). The denominator in equation 4 is introduced to normalize each trace of the signal by the first trace. Finally, the obtained dispersion image presents maxima that correspond to seismic events propagating with the slowness p at a frequency ω. For a given mode m propagating at a slowness $p_m(\omega)$ and a trace spacing of Δ_x, these maxima appear when (Russel, 1987; Forbriger, 2003b)

$$p(\omega) = p_m(\omega) + n_1 \frac{2\pi}{\omega\Delta_x}, \tag{5}$$

where n_1 is an integer. The maximum observed for $n_1 = 0$ is the main maximum corresponding to the mode m propagating at the slowness p_m in the wavefield. The other maxima ($n_1 \neq 0$) are aliased and depend on the spatial sampling Δ_x. Aliasing appears in the interval $0 \leq p \leq 2p_m$ at a frequency defined by

$$f(p_m) = \frac{1}{\Delta_x p_m}. \tag{6}$$

Conversely, the amplitude of the dispersion image is minimal when

$$p(\omega) = p_m(\omega) + n_2 \frac{2\pi}{\omega N_x \Delta_x}, \tag{7}$$

where n_2 is an integer, and $n_2 \neq 0, \pm N_x, \pm 2N_x$, etc. The resolution in slowness (half-distance between two minima) can then be defined as

$$\Delta_p = \frac{1}{f N_x \Delta_x}. \tag{8}$$

This relationship implies that the resolution of the dispersion image directly depends on the length of the seismic array ($N_x\Delta_x$) and also on the frequency f. The resolution decreases with the frequency, but it is independent of the phase velocity. The resolution of a given frequency is thus higher for an event propagating at a lower velocity. Furthermore, because the low-frequency (i.e., large wavelength) dispersion is influenced by the properties of the deepest layers, the investigation depth is directly linked to the resolution, and hence to the length of the seismic array.

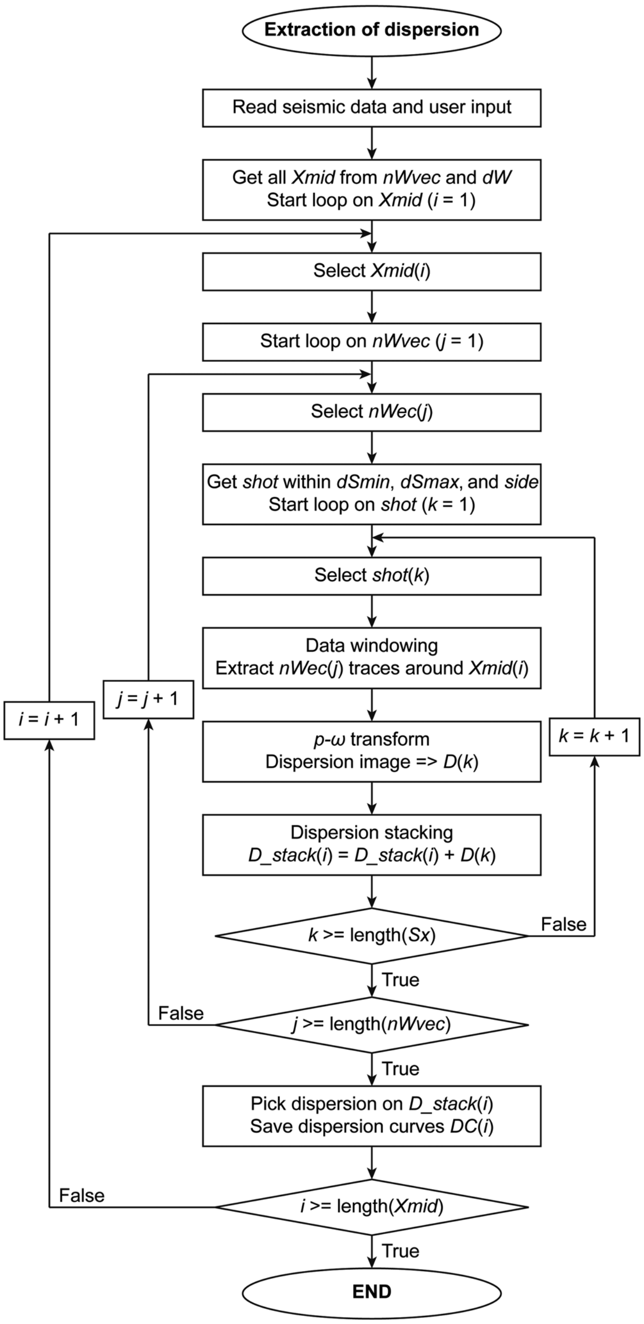

Figure 1. Flowchart of the dispersion extraction procedure.

Data windowing and dispersion stacking (module A)

For 2D applications, the length of the extraction spread is thus a key parameter that needs to be defined with care based on the desired lateral resolution and investigation depth. The spread has to be short enough to validate the 1D hypothesis (i.e., no or only small lateral variations below it) required for the inverse problem (Bodet et al., 2005), whereas alternatively it has to be large enough to ensure sufficient spectral resolution and record low-frequency dispersion data needed to increase the investigation depth (Bodet et al., 2009). Taking advantage of multishot acquisition setups, we implemented data windowing and dispersion stacking techniques (O'Neill et al., 2003; Neducza, 2007) to narrow down the lateral extent of dispersion measurements and increase the S/N necessary to perform 2D profiling. In SWIP, these techniques are performed according to the following workflow (Figure 2):

1) Select seismic data subsets centered on a specific position (Xmid) with window sizes defined by a vector nWvec containing the number of traces of each window.
2) Select shots illuminating the selected subsets with offsets (i.e., distance between the shot and the closest trace) ranging between the dSmin and dSmax traces on the left, right, or both sides of each subset.
3) Extract the selected subsets from the shot gathers for each shot/window size pair.
4) Transform the wavefield to the frequency-phase velocity domain (dispersion image) for each selected subset.
5) Normalize the amplitude spectrum at each frequency for each dispersion image.
6) Stack all normalized dispersion images computed at the same Xmid.
7) Shift the window of dW traces, and repeat steps 1–6 to the next Xmid.

As mentioned above, it is critical to find the best compromise between the investigation depth and the spectral and lateral resolution while keeping the 1D assumption valid for each extraction spread. It is thus recommended to start the analysis with trial-and-error tests (Pasquet et al., 2012) to determine the optimum windowing and stacking parameters, keeping in mind that no perfect criterion has yet been defined (Pérez Solano et al., 2014). The best window size (i.e., nWvec) should be determined after checking, for different window sizes, the validity of the 1D approximation for each shot/window size pair centered on a common Xmid (e.g., Bodet et al., 2005; Jongmans et al., 2009). The window size should be progressively decreased until the loss in spectral resolution becomes too high to justify the gain in lateral resolution. As shown in Figure 2, SWIP also allows one to stack dispersion extracted from different window sizes to help mitigate those issues. However, this option has not yet been extensively tested and requires further studies before being widely applied.

A similar procedure should be used for the choice of the shot-window offset range (i.e., dSmin and dSmax). Although stacking is meant to enhance the quality of dispersion images, mitigate the near-field effect, and facilitate dispersion picking, using noisy far-offset shots can have the opposite effect and deteriorate the final image quality. Finally, the shift between two successive extraction windows should be defined depending on the expected lateral variations in the studied medium. Although it can range from one trace spacing to several window lengths, using a large overlap (i.e., small dW) between two adjacent stacking windows will allow one to retrieve smoothly varying dispersion images and help with visual browsing when picking dispersion curves.

Dispersion picking and uncertainty estimation (module A)

On each stacked dispersion image, the coherent maxima associated with the different propagation modes are identified, picked, and saved as dispersion curves. These curves can either be picked manually, or with a semiautomatic procedure looking for the closest maxima around each pick. The measurement uncertainties associated with these dispersion curves depend directly on the resolution of the dispersion images and should be taken into account during the inversion. When field conditions (e.g., weather, funding, and manpower) prevent repeated measurements, it is impossible to estimate uncertainties with an experimental statistical analysis. To address such issues, O'Neill (2003) demonstrates that these uncertainties follow, at logarithmic scale, a frequency-dependent relationship proportional to the resolution envelope (and thus to the spread length), with a Gaussian distribution at high frequency (≥25 Hz), and a Lorentzian distribution (Bevington and Robinson, 2002) at low frequency (≤25 Hz). Hence, O'Neill (2003) proposes using the following algorithm:

1) Calculate the resolution in terms of phase velocity derived from the resolution in terms of slowness (equation 8)

$$\Delta_c(f) = \left| \frac{1}{\frac{1}{c(f)} - \frac{1}{2fN_x\Delta_x}} - \frac{1}{\frac{1}{c(f)} + \frac{1}{2fN_x\Delta_x}} \right|. \tag{9}$$

2) Calculate the absolute uncertainty by logarithmic reduction of the resolution

$$\delta_c(f) = 10^{-a}\Delta_c(f), \tag{10}$$

with a being the logarithmic reduction factor, usually 0.5 (O'Neill, 2003).

The dispersion curves and their associated uncertainties can then be resampled either in wavelength or frequency. A discretization in wavelength is generally recommended to invert depth-consistent data (Rix and Leipski, 1991; Wathelet et al., 2004). This also prevents one from giving excessive weight to high-frequency samples, which correspond only to the shallowest part of the medium. The frequency and wavelength ranges of the dispersion curves can be confined into reasonable boundaries using several criterions. As a first approach, dispersion curves can be limited down to frequencies at which the spectral amplitude of the shot gather becomes too low (Pasquet et al., 2015a, 2015b). Several authors (e.g., O'Neill, 2003; Bodet et al., 2005, 2009; Zywicki and Rix, 2005) also mention that wavelengths higher than 50% of the spread length should not be used to mitigate near-field effects and prevent velocity underestimation at low frequency. These recommendations are basic rules of thumb useful to prepare inversion parameterization and are mostly valid when using the fundamental mode only. Such limitations in wavelength have to be reconsidered when including higher

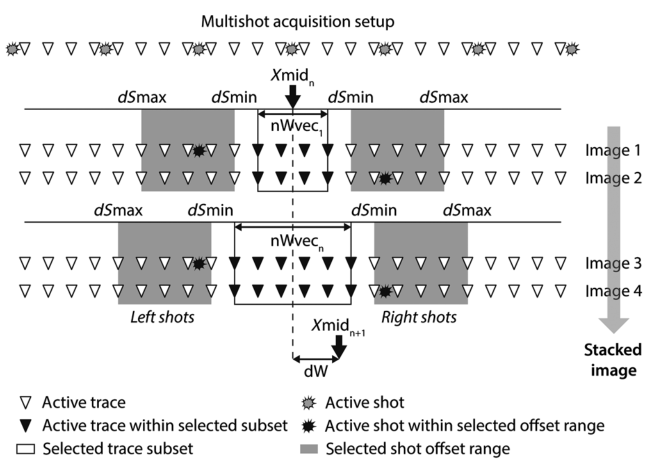

Figure 2. Data windowing and dispersion stacking workflow.

modes because they have a significant impact on the investigation depth and constrain the inversion (Gabriels et al., 1987; Xia et al., 2003). In SWIP, the resulting dispersion curves are eventually presented as phase velocity pseudosections (e.g., Strobbia et al., 2011; Haney and Douma, 2012; Boiero et al., 2013; Ezersky et al., 2013; Pasquet et al., 2015b). This representation is very convenient for quality control of picked dispersion and more particularly to check the lateral coherence in mode identification (Zhang and Chan, 2003; O'Neill and Matsuoka, 2005; Boaga et al., 2013; Ezersky et al., 2013).

Inversion of dispersion

Parameterization, forward modeling, and NA inversion are performed within the Dinver tool, part of the Geopsy open-source software package (Wathelet, 2017). Assuming a horizontally layered (1D) medium below each extraction window, SWIP performs a 1D inversion of dispersion curves obtained at each Xmid position. When a large overlap between two adjacent stacking windows (i.e., small dW) is chosen, stacking and windowing operations will naturally smooth lateral changes in dispersion data. In this case (recommended in SWIP), the use of lateral constraints between successive inversions is not necessary to retrieve smooth and coherent lateral variations of V_S (Strobbia et al., 2011). The dispersion inversion procedure is illustrated by the flowchart in Figure 3.

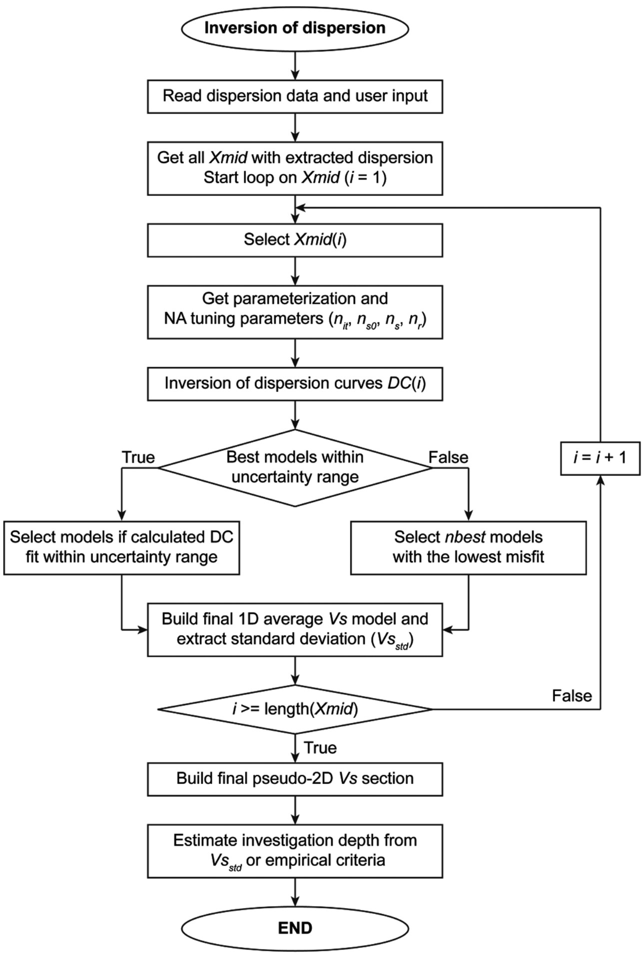

Figure 3. Flowchart of the dispersion inversion procedure.

Inversion parameterization (module B)

An appropriate choice of the parameters is considered fundamental to successfully performing the inversion (Socco and Strobbia, 2004; Renalier et al., 2010). Usually based on a priori knowledge (the presence of weathering gradients, sedimentary layers, low-velocity zone, etc.), the parameterization can be defined with several layers of fixed or varying thickness, velocities (V_P and V_S), and density. Velocities and density can be defined in each layer with various depth-dependent shapes (e.g., uniform, linear increase or decrease, power law) allowing a large range of possible models. The maximum half-space depth (HSD), defined by the number of layers and their maximum thickness, is of great importance because it depends on the poorly known investigation depth of the method. It is usually recommended, as a first step, to fix it to half of the maximum observed wavelength (O'Neill, 2003; Bodet et al., 2005). Because P-wave velocity and density have a weak constraint on SW dispersion, it is important to keep in mind that only the S-wave velocity profile can be interpreted from the inversion results (Der and Landisman, 1972; Russel, 1987). Although density can most of the time be set as uniform, it is recommended to use an identical layering for V_P and V_S.

As shown above, there are no specific limitations on the parameterization. An important number of layers (overparameterization) should be avoided, but the parameterization should still give some flexibility to the inversion algorithm (i.e., keeping the number of layers as low as possible). Yet, the variability of the generated models should remain important enough for the modeled dispersion to fit possibly complex extracted data. In such situations, finding a good compromise is always a delicate task, particularly when the measured dispersion curves show variability along the profile. In the absence of strong a priori information, it is recommended to

1) Select several typical Xmid positions along the line in terms of dispersion patterns.
2) For each of these Xmid positions, build the simplest possible parameterization, with the lowest possible number of layers.
3) Run the inversions and, step by step, give more degrees of freedom to the algorithm by adding layers (and/or by extending parameter ranges) if the dispersion curves are not sufficiently matched (Wathelet et al., 2004).

When a priori information about the probed subsurface is available along the line (e.g., from other geophysical, geologic, or log data), the inversion can consist of the optimization of an a priori model, rather than the exploration of all possible solutions. In that case, we recommend applying the following parameterization strategy:

1) Select several typical Xmid positions along the line in terms of a priori knowledge.
2) Build velocity structures based on a priori information with reduced thickness and velocity ranges.
3) Perform forward modeling to roughly estimate if these structures present the appropriate number of layers and velocity ranges.
4) Run the inversions and, step by step, adapt degrees of freedom given to the algorithm if the dispersion curves tend to be correctly matched, to converge to a satisfying parameterization according to a priori information.

When studying variations of V_P/V_S or Poisson's ratio (Pasquet et al., 2015b) and when the acquisition setup allows one to perform

P-wave refraction tomography, SWIP can create a semiautomatic parameterization based on refraction results. In such a case, V_P soundings are extracted at each Xmid position from the tomography model and resampled according to the desired parameter space discretization in depth. This average value can then be used to fix V_P in each layer or to estimate a limited and realistic variation range.

Neighborhood algorithm inversion (module C)

The inversion is performed with the neighborhood algorithm (NA) developed by Sambridge (1999a) and implemented for near-surface applications by Wathelet et al. (2004) and Wathelet (2008) within the Dinver tool. Theoretical dispersion curves are computed from the elastic parameters using the Thomson-Haskell matrix propagator technique (Thomson, 1950; Haskell, 1953) as implemented by Dunkin (1965). NA then makes use of Voronoi cells to iteratively sample the parameter space (such as V_P, V_S, density, and thickness of each layer). At the first iteration, NA randomly generates n_{s0} models in the parameter space and calculates the following misfit function (MF):

$$\mathrm{MF} = \sqrt{\sum_{i=1}^{N_f} \frac{(V_{\mathrm{cal}_i} - V_{\mathrm{obs}_i})^2}{N_f \sigma_i^2}}, \tag{11}$$

with V_{cal_i} and V_{obs_i} being the calculated and observed phase velocities at each frequency f_i, N_f the number of frequency samples, and σ_i the phase-velocity measurement uncertainty at each frequency f_i.

The parameter space is then divided into n_{s0} Voronoi cells centered on each generated model, with the boundaries in each parameter direction being equidistant from the nearest neighbor model. The n_r best cells (i.e., with the lowest MF) are then selected, within which n_s/n_r new models are randomly generated. The n_s new models are finally added to the previous ones, updating the Voronoi cells distribution. This operation is repeated for n_{it} iterations until reaching $n_{s0} + (n_s n_{it})$ generated models. The use of Voronoi cells allows one to adapt the parameter space along successive iterations, unlike classical Monte Carlo inversion schemes, which search for new models along a predefined grid of parameters (Wathelet, 2008). Depending on the tuning parameters used, the NA can be considered very exploratory (high n_{s0}, n_s, and n_r) or on the contrary tend to local optimization (low n_{s0}, n_s, and n_r). The main goal is to find a compromise that allows for the generation of a large enough number of models sweeping the whole parameter space, then to converge toward the more probable areas without reaching local minima too quickly, while limiting the processing time.

NA is consequently not a purely random approach. The generation of models is iteratively guided toward the area of lowest MF. The advantage is obviously a lower computational cost compared with completely random methods. Yet it has to be used with care because it does not prevent falling into the local minima of the MF, more particularly when using a restricted parameter space with poor a priori information. As already suggested regarding the parameterization, we suggest establishing the inversion strategy based on the strength of the available a priori information. In the case of poor knowledge about the investigated structures, it is recommended to tune the NA to be as exploratory as possible. Then, when the areas of the MF in which the NA tends to converge seem repetitive with an important number of models and a large parameter space, the inversion can be retuned as more optimizing until finding the best compromise between the number of generated models and the processing time. The flexibility offered by the NA in terms of tuning as well as the variety of provided outputs and associated estimators make it a rather versatile and convenient tool for such SW applications (e.g., Sambridge, 1999a, 1999b; Wathelet et al., 2004; Wathelet, 2008).

Final 1D V_S model estimation (module C)

Thousands of models can be generated for each Xmid with the NA, allowing the appraisal of an a posteriori estimate of the model error. SWIP allows for a detailed presentation of 1D inversion results at each Xmid position. Computed dispersion data and models are represented according to their misfit with different color scales for accepted and rejected models (Endrun et al., 2008). This layout is useful to visually estimate the modal dispersion of the explored parameter space and fairly interpret extracted results. Two options are offered to select the accepted models: (1) keeping the n_{best} models with the lowest misfits and (2) or selecting all models whose calculated dispersion curves fit the observed data within the uncertainty range. Using all selected models, we then propose to build a final average model either by taking the mean value of each model parameter, or by weighting the different parameters according to each model's misfit value. To correctly estimate the a posteriori model error, it is recommended to select at least 500–1000 models.

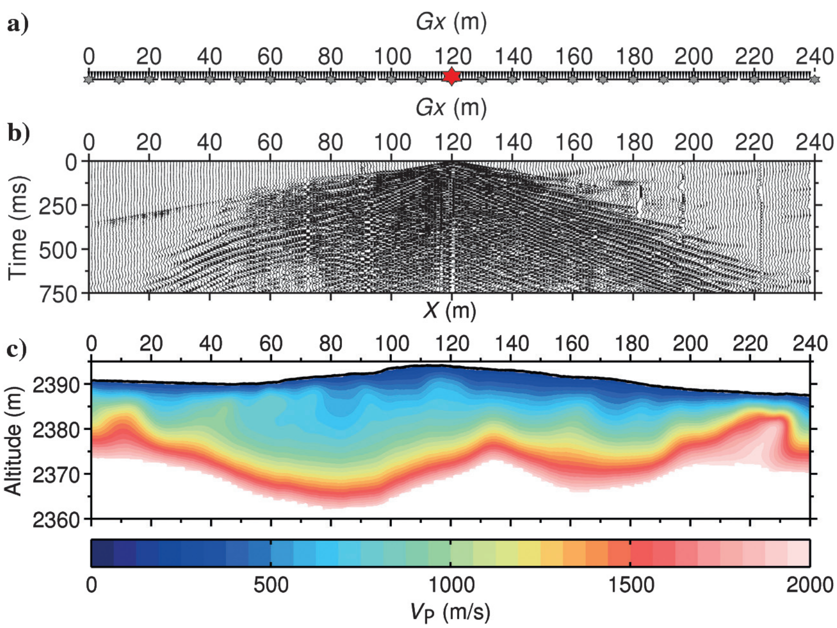

Figure 4. (a) Layout of the seismic acquisition setup, with 240 geophones (gray triangles) spaced every 1 m and 25 shots (gray stars) spaced every 10 m. (b) Example of a shot gather for a source located at 120 m (red star in a). (c) Final V_P model obtained from P-wave traveltime tomography. The topography extracted from airborne LiDAR data is represented with a solid black line.

When selecting models within the uncertainty range, the inversion may have to be run several times with different NA tuning parameters until obtaining an acceptable number of models fitting within the uncertainties. Ultimately, this final average model could be used as a starting model in a linearized inversion scheme, as proposed by Socco and Boiero (2008). It is worth mentioning that SWIP does not yet provide specific tools to quantitatively draw inferences from the estimated misfit (Mosegaard and Tarantola, 1995; Sambridge, 2001; Sambridge and Mosegaard, 2002). As for SW dispersion inversion in general, various approaches existing in the literature (Sambridge, 1999b; Wathelet et al., 2004; Socco and Boiero, 2008; Wathelet, 2008) could be implemented to exploit the full wealth of NA outputs.

Quality control and pseudo-2D V_S section extraction (modules D1 and D2)

Despite these limitations, SWIP provides an extensive selection of postinversion quality-control tools. The software, for instance, offers comparison of pseudosections of picked and calculated phase velocities, along with their residuals at each *X*mid position. Such representation of the data, adapted from electrical resistivity tomography codes, is very useful to review the inversion fit along the acquisition line and check for possible misinterpretations. The coherence of the 1D V_S models eventually extracted at each *X*mid can also be verified by superimposing theoretical dispersion curves on dispersion images (Pasquet et al., 2014). This particular representation helps point out possible mode misidentification and checking if originally discarded higher modes could have been picked and inverted. Furthermore, it is possible to represent the misfit value for each pair of inverted parameters and characterize the resolution and sensitivity of each of those parameters (Wathelet et al., 2004).

Each final 1D V_S model can finally be represented at its corresponding *X*mid position to create a pseudo-2D section of V_S. Although the investigation depth of 1D V_S models is usually considered equal to the half of the maximum observed wavelength (Socco and Strobbia, 2004), we also propose here to take advantage of the Monte Carlo approach to estimate the investigation depth from the standard deviation of all models selected after the NA inversion. For each final 1D V_S model, we propose to define the depth of investigation when the standard deviation reaches a user-defined threshold above which V_S is considered unconstrained. SWIP users should then keep in mind that this final pseudo-2D V_S section only represents merged averages (and hence smooth) of all possible solutions at each *X*mid (Mosegaard and Tarantola, 1995). In most cases, the final models interpreted from such a data fitting process will, by definition, only consist of an estimation of the true V_S structures. However, the outputs provided by the inversion can be used to

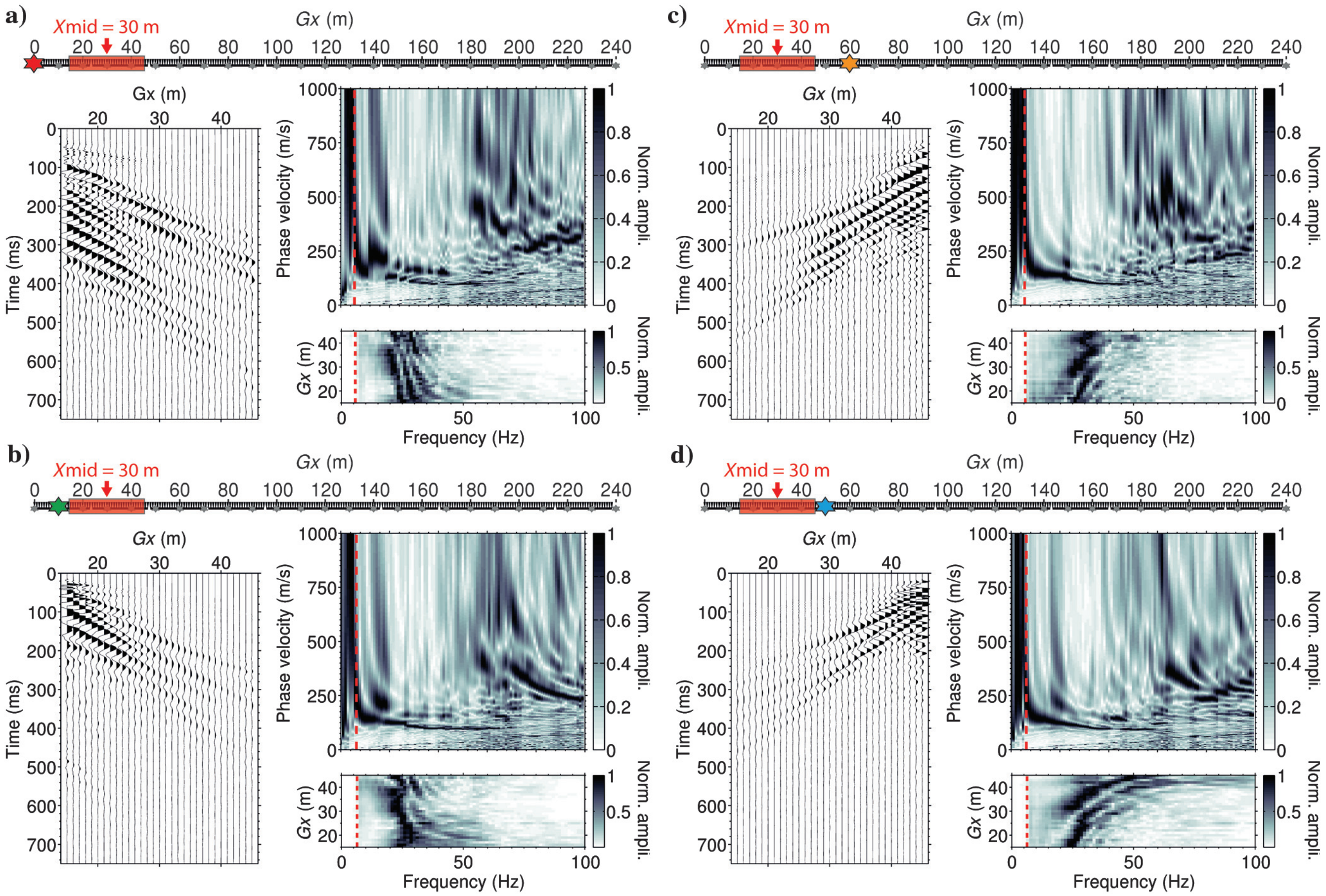

Figure 5. Extraction of single dispersion images for a 31 trace window centered at *X*mid = 30 m, using shots located at (a) 0 m, (b) 10 m, (c) 50 m, and (d) 60 m. On each inset, windowed shot gathers are on the left, corresponding spectrograms are at the bottom right, and computed dispersion images are at the top right. The dashed red lines on the spectrograms and dispersion images correspond to automatic low-cut frequencies defined from the spectrogram amplitude.

address specific questions such as the depth or location of specific interfaces, the existence of velocity anomalies (low-velocity layers, for instance), or the occurrence of strong lateral variations, as shown in the following field example.

FIELD EXAMPLE

Description of the geophysical survey

We present here the results of a geophysical survey carried out in Yellowstone National Park (USA), in the Obsidian Pool Thermal Area. It is located in the eastern part of the Yellowstone caldera, within the Mud Volcano thermal area, which mainly consists of rhyolitic ash flow tuff covered with varying thicknesses of glacial silts, sand, and gravel (Christiansen and Blank, 1975). The area is also characterized by extensive diffuse degassing of CO_2 through soils (Werner et al., 2000) and hosts several isolated thermal features, mostly of acid-sulfate composition with water temperatures between 21.9°C and 84.0°C (Hurwitz et al., 2012).

Seismic measurements were performed in this site to study shallow hydrothermal systems, characterize fluid pathways and improve understanding of the depths of separation of steam from liquid water. Seismic data were collected in July 2016 along a south-southwest–north-northeast transect, crossing a heat-flow anomaly (Hurwitz et al., 2012) between 50 and 120 m and a degassing feature (Pasquet et al., 2016b) between 86 and 96 m. We used 10 24-channel Geometrics Geode seismographs with 4.5 Hz vertical component geophones spaced every 1 m, so as to obtain a 239 m long profile (Figure 4a). Twenty-five shot gathers were recorded every 10 m using a 5.4 kg sledgehammer source swung onto a metal plate. The plate was hit five times at each position to increase the S/N. The sampling rate was 0.125 ms, and the recording time was 0.75 s to include the full SW wavefield. The hydrothermal features and the acquisition line were GPS surveyed, and the topography was extracted from airborne LiDAR data (OpenTopography, 2017).

First-arrival times were picked manually on the shot gathers (Figure 4b) and inverted for P-wave velocity using a MATLAB traveltime tomography code (St. Clair, 2015). To estimate the sensitivity and the depth of investigation of our model, we repeated the inversions for a range of 100 starting models with different velocity gradients and surface velocities (St. Clair et al., 2015). All models presenting a satisfactory fit to the data were used to build an average final model with a depth of investigation defined using a threshold on the standard deviation of all accepted models (Pasquet et al., 2016b). The final V_P model shows smoothly varying velocities ranging between 100 and 2000 m/s, with an approximately 5 m thick, low-velocity layer at the surface (Figure 4c).

Extraction of dispersion

After converting raw SEG2 data into the SU format, we used SWIP to extract dispersion images from the seismic data. Following the recommendations formulated above, we performed trial-and-error tests with different window sizes and source-window offsets. We eventually used a 30 m (nWvec = 31) window with source-window offsets ranging between 0 and 20 m on both sides of the window (dSmin = 0 and dSmax = 20). Though near-field effects can appear when using very short offsets (i.e., dSmin = 0), stacking dispersion images with larger offset shots should mitigate this prob-

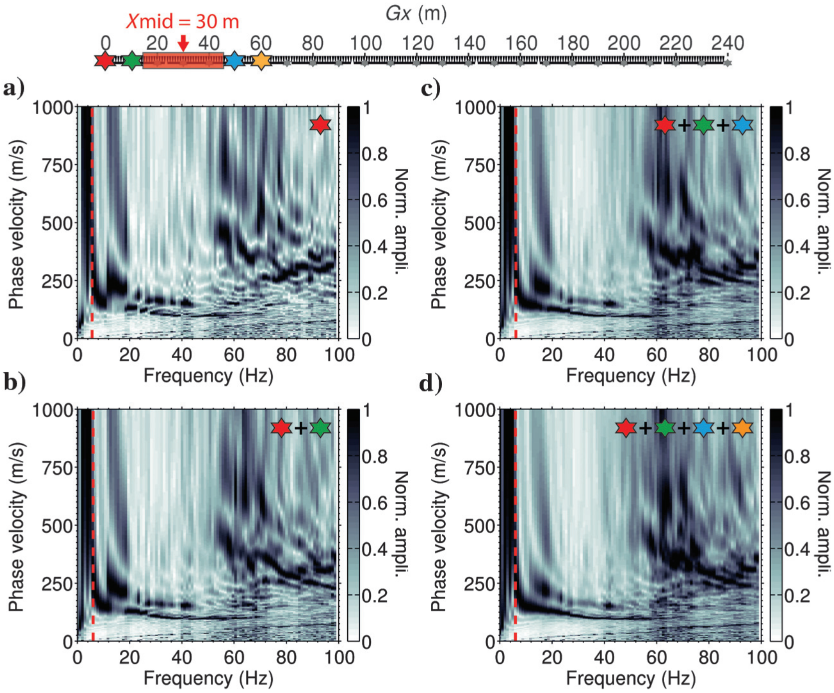

Figure 6. (a-d) Successive stacking of the single dispersion images represented in Figure 5a–5d.

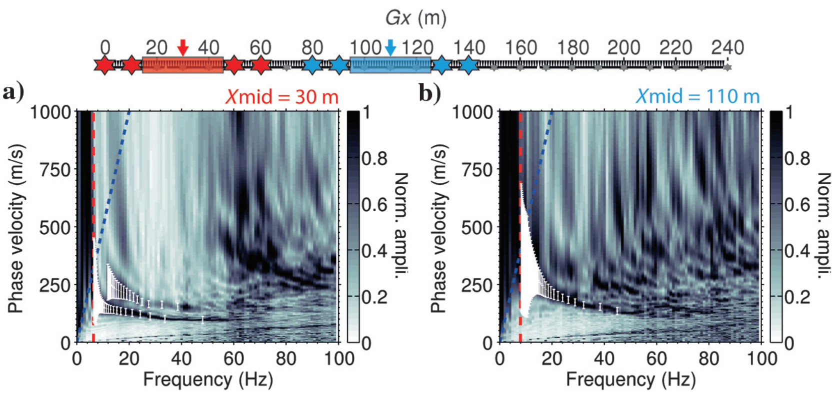

Figure 7. Stacked dispersion images extracted at (a) Xmid = 30 m and (b) Xmid = 110 m with picked dispersion curves (white error bars) of the fundamental (0) and first higher (1) modes. The uncertainty range is defined according to the workflow described in O'Neill (2003). Dispersion curves are limited down to a frequency defined with a spectral amplitude threshold of 2.5% (dashed red line), or up to a wavelength of 50 m (dashed blue line).

lem (Neducza, 2007). Furthermore, the use of higher modes and larger uncertainties at low frequencies (i.e., where near-field effects perturb the data the most) also helps dealing with the underestimation of phase velocities (Bodet et al., 2009). The first and last windows were centered at 15 and 224 m, respectively, with three to six shots illuminating each window. For each window position (Xmid), dispersion images computed from each of these shots were first compared (Figure 5) to confirm the validity of the 1D approximation below each spread. The clear consistency observed between single dispersion images at each Xmid position authorized the stacking of those images.

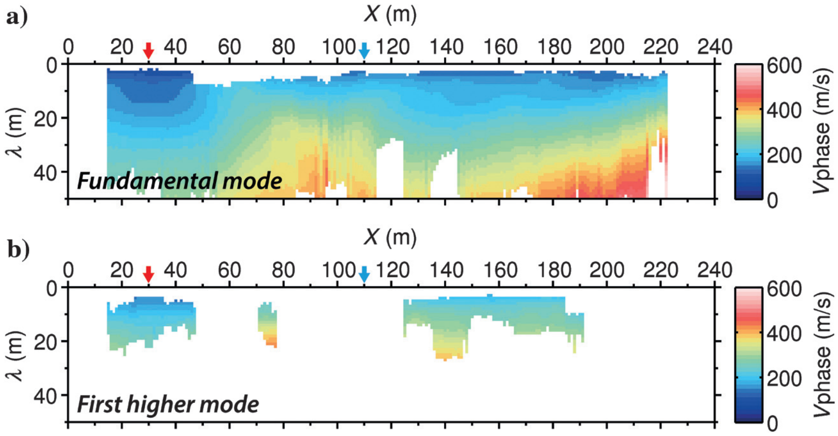

Figure 8. Pseudosections of SW phase velocity picked for (a) the fundamental and (b) first higher modes along the line after dispersion stacking, represented as a function of the wavelength λ and the spread mid-point position.

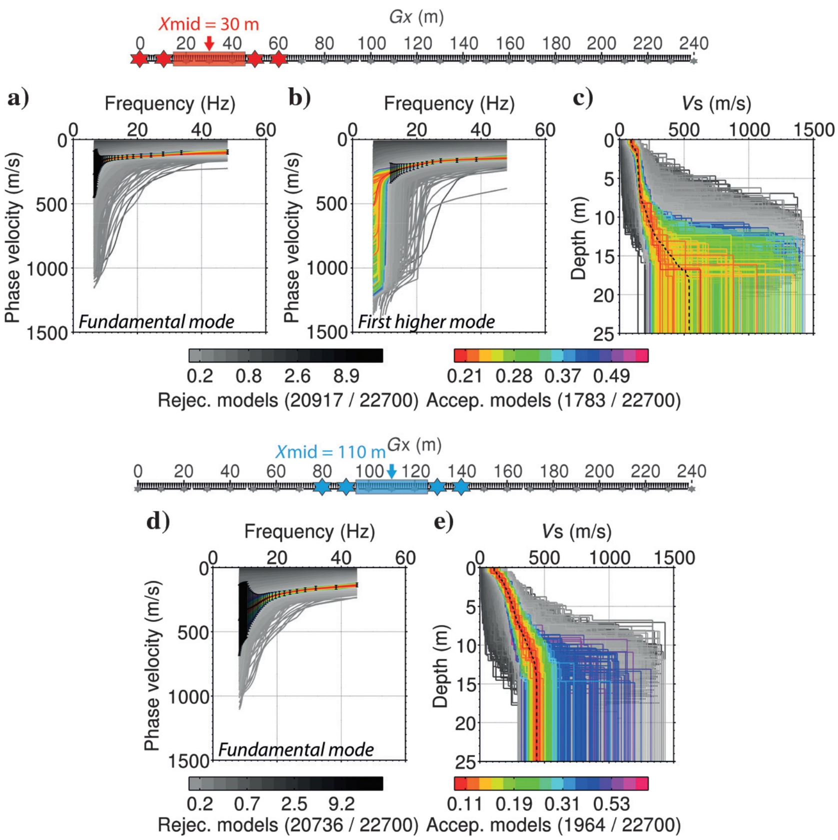

Figure 9. Results of 1D NA inversions of dispersion data (black error bars) at Xmid = 30 m ([a] fundamental and [b] first higher modes) and Xmid = 110 m ([d] fundamental mode). Resulting V_S models are represented for (c) Xmid = 30 m and (e) Xmid = 110 m, along with a misfit-weighted velocity structure (dashed black lines) built from the average parameters of all accepted models. Calculated dispersion and corresponding models are represented with misfit-based color and gray scales for accepted and rejected models, respectively.

In the example presented in Figure 6 and all along the line, stacking of dispersion images clearly enhanced the S/N and helped in the identification of SW propagation modes. The window was then shifted 1 m along the acquisition profile ($dW = 1$) to obtain 210 evenly spaced dispersion images at each Xmid position. The large overlap between two adjacent stacking windows provided smoothly varying dispersion images and helped the identification of propagation modes during the picking process.

We eventually picked coherent maxima associated with the identified propagation modes on each stacked dispersion image obtained along the line. Adjacent dispersion images were displayed during picking to follow the lateral evolution of different modes and to avoid mode misidentification. Dispersion curves were automatically cut down to frequencies at which the spectral amplitude of the shot gather became too low. We used a threshold of 2.5% of the normalized amplitude to define this frequency for each single dispersion image, and then we used the average frequency at each Xmid to determine the low cut of the dispersion curve. The cut-off frequency ranges between 5 and 10 Hz along the line, with the corresponding wavelength varying from 25 to 50 m. These dispersion curves were finally extracted with their associated uncertainty in phase velocity estimated with equations 9 and 10, then resampled in wavelength every 1 m from 0 to 50 m (Figure 7).

The fundamental mode (0) of SWs was clearly identified all along the line, whereas the first higher mode (1) was only identified from 15 to 47 m, 71 to 77 m, and 125 to 191 m. To visually inspect the lateral consistency of picked modes, we represented dispersion curves as SW phase velocity pseudosections (Figure 8). Both pseudosections present smooth lateral variations with phase velocities ranging between 100 and 600 m/s. Higher phase velocities are observed on the fundamental mode between 60 and 120 m and at the end of the line. The whole dispersion extraction procedure (Figure 1) was performed over the 210 Xmid in approximately 45 min using a laptop with a quad-core 2.10 GHz processor and 16 GB of RAM (not including the picking process that can take up to a few hours).

Inversion of dispersion

Assuming a 1D medium below each extraction window, we then used SWIP to perform 1D NA inversions of dispersion curves extracted at each Xmid. We applied the trial-and-error strategy formulated above, testing different parameterizations and NA tuning parameters. We finally used a parameterization with a stack of 10 layers overlaying the half-space to look for smooth nonlinear velocity gradients, as expected with regard to P-wave refraction results and a priori geologic knowledge (unconsolidated sediments and weathering gradient). The thickness of each layer was allowed to range from 0.5 to 2.5 m. We fixed the maximum HSD to half of the maximum wavelength observed along the entire line (25 m). The valid parameter range for sampling velocities was 10–2500 m/s for V_S with velocities constrained to only increase with depth based on a priori geologic information. The range of V_P was defined by tomography results after extracting at each Xmid position an average V_P value at each 2.5 m thick slice of the refraction tomography model (Figure 4c). This average value was then used to reduce the range of possible V_P in each layer of the inversion parameterization. Poisson's ratio was defined between 0.1 and 0.5 to prevent unrealistic V_S values, and the density was set as uniform ($2000\ \mathrm{kg/m^3}$). Except for V_P that were defined to closely follow variations of the P-wave tomography model, we used an identical parameterization for all 1D inversions, with no lateral constraints between successive inversions, relying on the important overlap of adjacent extraction windows.

For each Xmid position, we performed two separate runs of NA with $n_{it} = 150$, $n_{s0} = 100$, $n_s = 75$, and $n_r = 50$, so as to generate 22,700 models (Figure 9). After each 1D inversion, we selected models matching the observed data within the uncertainty range (i.e., all samples of the theoretical dispersion curves calculated from the model fitted the observed data within the uncertainty range). Average parameters of all accepted models were then used to build a misfit-weighted velocity structure associated with the center of the extraction window. Using this average V_S model and the V_P model extracted from tomography results at each Xmid position, we computed theoretical dispersion curves to check their fit with the observed dispersion (Figure 10) and confirm the acceptability of the average 1D V_S.

We finally compared observed and calculated phase velocity for fundamental and first higher modes at each Xmid position, and computed their residuals to verify the overall consistency of the inversion along the profile (Figure 11). The final model has a root-mean-square of 13.9 m/s, with 94.7% of the samples with normalized phase-velocity residuals less than 7.4%. The whole dispersion inversion procedure (Figure 3) was performed over the 210 Xmid in approximately 4 h using a laptop with a quad-core 2.10 GHz processor and 16 GB of RAM.

We then estimated the investigation depth for each Xmid position from the standard deviation of all selected V_S models. We used a threshold of 150 m/s on the standard deviation of V_S to determine

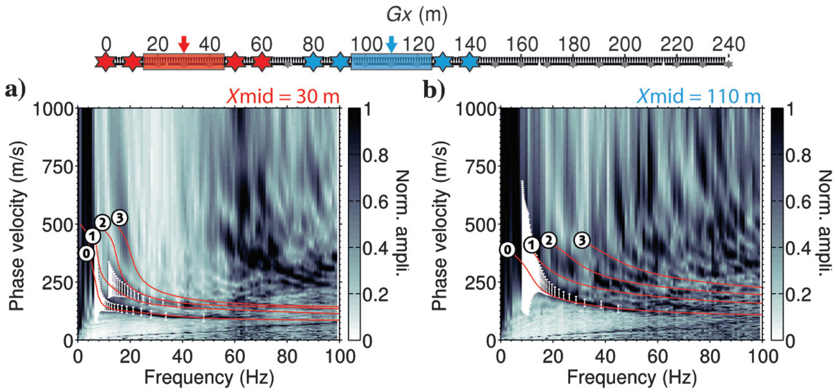

Figure 10. Stacked dispersion images extracted at (a) Xmid = 30 m and (b) Xmid = 110 m with picked (white error bars) and calculated (solid red lines) dispersion curves represented for the fundamental (0), the first (1), second (2), and third (3) higher modes.

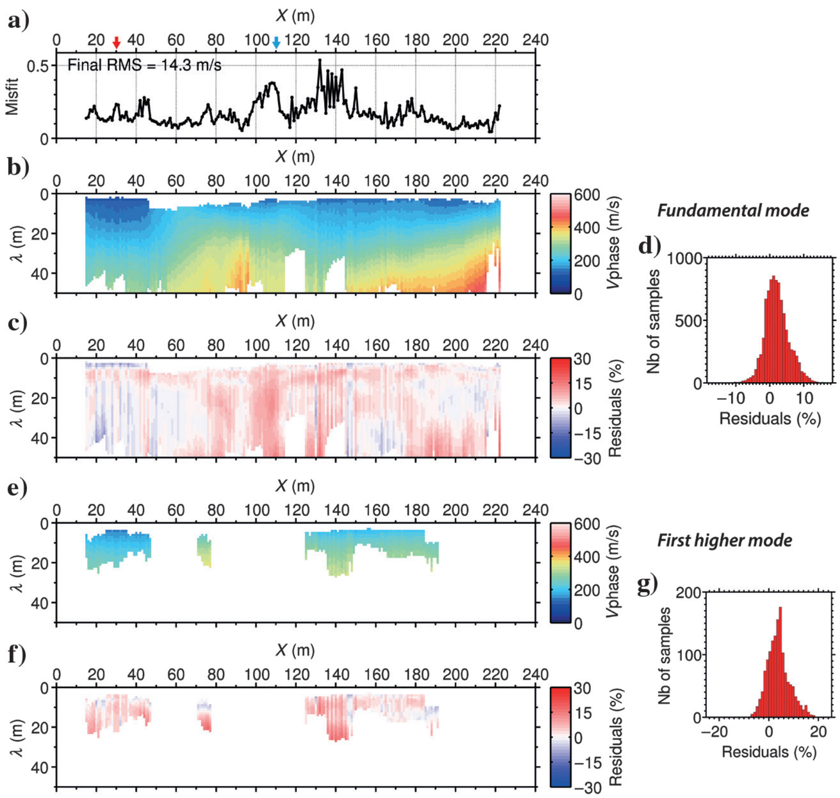

Figure 11. (a) Misfit value calculated with equation 11 for each 1D NA inversion along the line. (b) Pseudosection of calculated phase velocity for the fundamental mode. (c) Pseudosection of phase-velocity residuals for the fundamental mode. (d) Histogram of residuals for the fundamental mode. (e) Pseudosection of calculated phase velocity for the first higher mode. (f) Pseudosection of phase-velocity residuals for the first higher mode. (g) Histogram of residuals for the first higher mode.

the investigation depth and limit the extent of the velocity model in depth (Figure 12a). Finally, each 1D V_S model was represented at its corresponding extraction position to build a pseudo-2D section of V_S (Figure 12b). The V_S model is characterized by velocities ranging between 50 and 600 m/s, with higher shallow V_S below the heat-flow anomaly observed between 50 and 120 m. Although the V_S model has a lower investigation depth than the V_P model, it provides more information regarding the lateral variations of shallow layers' velocities due to the intrinsic smoothing of tomographic inversion and the substantial horizontal component of P-wave travel paths.

When a V_P model is available from P-wave tomography for instance, SWIP can also calculate Poisson's ratio, which is known to help identify different lithology or water/gas saturation changes in the subsurface (Pasquet et al., 2015a, 2016b). Using the inverted V_P (Figure 4c) and V_S (Figure 12b) models, we computed Poisson's ratio ν as

$$\nu = \frac{V_P^2 - 2V_S^2}{2(V_P^2 - V_S^2)}. \tag{12}$$

Poisson's ratio (Figure 13) shows values ranging between 0.3 and 0.5, which are typical of nonsaturated and saturated media, respectively. Poisson's ratio is predominantly between 0.45 and 0.5, indicating the high water content for most of the subsurface, except in the highest part of the hill. Lower Poisson's ratio values are also observed at depths below the degassing area visible at the surface, illustrating the ability of Poisson's ratio to map the shallow "plumbing" structure of hydrothermal systems and efficiently constrain gas versus water saturation at depth. Furthermore, this interpretation is in good agreement with the results of recent geophysical investigations conducted at the same site by Pasquet et al. (2016b), where rock-physics modeling highlighted lower saturation in the degassing area.

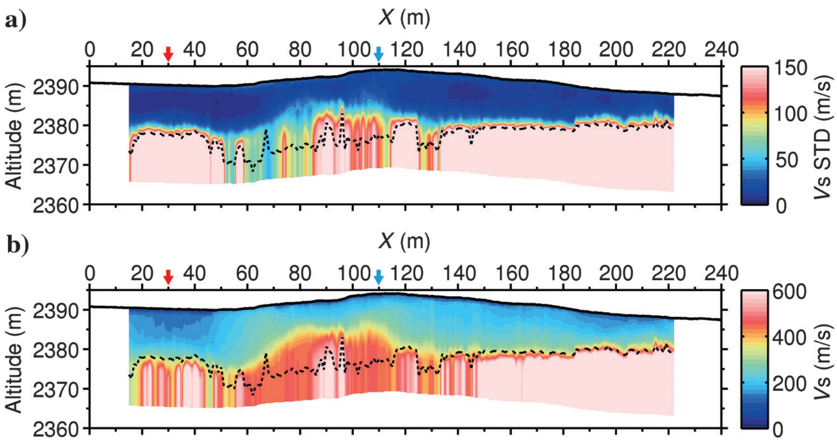

Figure 12. (a) Pseudo-2D section of V_S standard deviation computed from accepted models at each Xmid position along the line. (b) Pseudo-2D section of average V_S computed from accepted models at each Xmid position along the line. The dashed black line corresponds to the depth of investigation estimated with a V_S standard deviation threshold of 150 m/s. The topography extracted from airborne LiDAR data is represented with a solid black line.

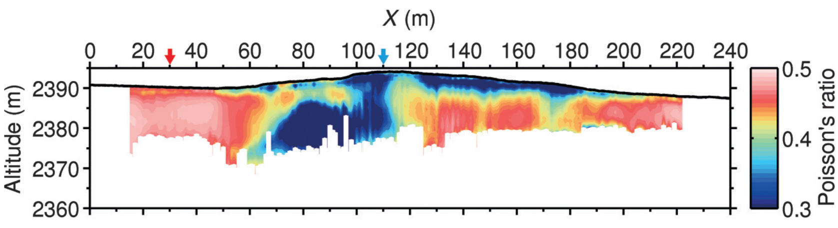

Figure 13. Poisson's ratio computed from P-wave tomography V_P and SW dispersion inversion V_S and masked below the depth of investigation estimated from V_S standard deviation. The topography extracted from airborne LiDAR data is represented with a solid black line.

CONCLUSION

SWIP is an integrated open-source MATLAB-based package that performs, within the same framework, SW inversion and profiling for the 1D to 2D imaging of V_S. It can be used with any kind of active-source near-surface seismic data collected along linear profiles, and it is particularly adapted (but not limited) to processing seismic data originally recorded to estimate V_P from P-wave refraction tomography. Each step of its workflow involves up-to-date processing and inversion techniques, integrated within five MATLAB modules automatically calling the necessary functions and softwares.

SWIP takes advantage of multishot acquisition setups to retrieve the lateral variations of SW dispersion (i.e., Rayleigh or Love depending on the source and geophone component), using shot-gather windowing and dispersion stacking techniques. These techniques clearly enhance S/N and make it possible to extract local dispersion images along the acquisition profile. The dispersion curves are consequently picked for each window with the associated uncertainties in phase velocities taking into account typical low-frequency discrepancies due to the limited spectral resolution of the method and near-offset effects. These curves are then represented as phase-velocity pseudo sections to enable convenient quality control of picked dispersion and lateral coherence in mode identification. The recommended use of a large overlap between two adjacent stacking windows provides naturally smooth changes in the dispersion measurements along the acquisition line; hence, inverting dispersion data for a pseudo-2D V_S section does not require the use of lateral constraints. Instead, SWIP uses a Monte Carlo inversion approach, with a choice of user-defined or refraction tomography-based parameterization, to retrieve 1D V_S models for each extraction window. Two options are then offered to select accepted models and build a final average model: (1) keeping the n_{best} models with the lowest misfits or (2) selecting all models whose calculated dispersion curves fit the observed data within the uncertainty range. In both cases, the final model can be built either by taking the mean value of each model parameter, or by weighting the different parameters according to the misfit value of each model. We finally merge all the final 1D V_S models into a pseudo-2D section of V_S, with a suggested investigation depth estimated from the standard deviation of each *X*mid accepted models.

Each step of SWIP's workflow provides ready-to-use outputs with extensive quality control tools, as illustrated in a field example. Seismic data collected with a single acquisition setup in Yellowstone National Park (USA) were processed to demonstrate the benefits of combining P-wave refraction tomography and SW dispersion inversion. In this example, the V_S model shows strong lateral variations that are not visible on the V_P model (due to strong saturation variations). Furthermore, the Poisson's ratio calculated from these two models, and more particularly its contrasts, clearly highlights gas pathways in the subsurface consistent with degassing observed at the surface. With these results, we demonstrated SWIP's versatility and robust usage and showed how it can provide supplementary information from existing seismic data sets. Nonetheless, some of the implemented features still require additional investigation before being systematically applied in further studies (e.g., optimum stacking and windowing parameters, refraction-based parameterization, and multiwindow size stacking). With this in mind, the open implementation of the software will also allow any user to suggest (and/or implement) alternative approaches for the extraction (e.g., CMPCC, Gaussian window, f-k transform, etc.) or the inversion (e.g., linearized, laterally constrained, or other Monte Carlo scheme) of SW dispersion.

ACKNOWLEDGMENTS

We kindly thank M. Dangeard, A. Dhemaied, I. Rahmania, and R. Callahan for helping to improve SWIP during its development and for proofreading the manuscript. We also thank B. Benjumea, C. Huerta, and two anonymous reviewers for their constructive comments on the manuscript. Finally, we gratefully acknowledge S. Holbrook and the Wyoming Center for Environmental Hydrology and Geophysics for providing the seismic data presented in this work. These data are available through the University of Wyoming Data Repository at https://doi.org/10.15786/M21S3V and can be used to reproduce the figures presented here by following the instructions provided in the SWIP user's guide. This work was funded by the CNRS, the PIREN-Seine program, the CRITEX ANR-11-EQPX-0011 project, and the SOERE-H+ hydrogeologic network. It was also supported by the Wyoming Experimental Program to Stimulate Competitive Research and National Science Foundation under award EPS-1208909.

REFERENCES

Aki, K., and P. G. Richards, 1980, Quantitative seismology: University Science Books.

Beaty, K. S., D. R. Schmitt, and M. Sacchi, 2002, Simulated annealing inversion of multimode Rayleigh wave dispersion curves for geological structure: Geophysical Journal International, **151**, 622–631, doi: 10.1046/j.1365-246X.2002.01809.

Bergamo, P., D. Boiero, and L. V. Socco, 2012, Retrieving 2D structures from surface-wave data by means of space-varying spatial windowing: Geophysics, **77**, no. 4, EN39–EN51, doi: 10.1190/geo2012-0031.1.

Bergamo, P., B. Dashwood, S. Uhlemann, R. Swift, J. Chambers, D. Gunn, and S. Donohue, 2016a, Time-lapse monitoring of climate effects on earthworks using surface waves: Geophysics, **81**, no. 2, EN1–EN15, doi: 10.1190/geo2015-0275.1.

Bergamo, P., B. Dashwood, S. Uhlemann, R. Swift, J. E. Chambers, D. A. Gunn, and S. Donohue, 2016b, Time-lapse monitoring of fluid-induced geophysical property variations within an unstable earthwork using P-wave refraction: Geophysics, **81**, no. 4, EN17–EN27, doi: 10.1190/geo2015-0276.1.

Bergamo, P., and L. Socco, 2016, P- and S-wave velocity models of shallow dry sand formations from surface wave multimodal inversion: Geophysics, **81**, no. 4, R197–R209, doi: 10.1190/geo2015-0542.1.

Bevington, P. R., and D. K. Robinson, 2002, Data reduction and error analysis for the physical sciences: McGraw Hill Higher Education.

Boaga, J., G. Cassiani, C. Strobbia, and G. Vignoli, 2013, Mode misidentification in Rayleigh waves: Ellipticity as a cause and a cure: Geophysics, **78**, no. 4, EN17–EN28, doi: 10.1190/geo2012-0194.1.

Bodet, L., O. Abraham, and D. Clorennec, 2009, Near-offset effects on Rayleigh-wave dispersion measurements: Physical modeling: Journal of Applied Geophysics, **68**, 95–103, doi: 10.1016/j.jappgeo.2009.02.012.

Bodet, L., K. van Wijk, A. Bitri, O. Abraham, P. Côte, G. Grandjean, and D. Leparoux, 2005, Surface-wave inversion limitations from laser-Doppler physical modeling: Journal of Environmental and Engineering Geophysics, **10**, 151–162, doi: 10.2113/JEEG10.2.151.

Bohlen, T., S. Kugler, G. Klein, and F. Theilen, 2004, 1.5D inversion of lateral variation of Scholte-wave dispersion: Geophysics, **69**, 330–344, doi: 10.1190/1.1707052.

Boiero, D., and L. V. Socco, 2010, Retrieving lateral variations from surface wave dispersion curves: Geophysical Prospecting, **58**, 977–996.

Boiero, D., and L. V. Socco, 2011, The meaning of surface wave dispersion curves in weakly laterally varying structures: Near Surface Geophysics, **9**, 561–570, doi: 10.3997/1873-0604.2011042.

Boiero, D., L. V. Socco, S. Stocco, and R. Wisén, 2013, Bedrock mapping in shallow environments using surface-wave analysis: The Leading Edge, **32**, 664–672, doi: 10.1190/tle32060664.1.

Cardarelli, E., M. Cercato, and G. De Donno, 2014, Characterization of an earth-filled dam through the combined use of electrical resistivity tomography, P- and SH-wave seismic tomography and surface wave data: Journal of Applied Geophysics, **106**, 87–95, doi: 10.1016/j.jappgeo.2014.04.007.

Christiansen, R. L., and H. R. Blank, 1975, Geologic map of the Canyon Village quadrangle, Yellowstone National Park, Wyoming: USGS Numbered Series 1192.

Dangeard, M., S. Pasquet, L. Bodet, R. Guérin, L. Longuevergne, and J. Thiesson, 2016, Temporal variations of near-surface seismic data at the Ploemeur (France) hydrogeological observatory: Presented at the Near Surface Geoscience 2016 — 22nd European Meeting of Environmental and Engineering Geophysics, EAGE.

Der, Z. A., and M. Landisman, 1972, Theory for errors, resolution, and separation of unknown variables in inverse problems, with application to the mantle and the crust in southern Africa and Scandinavia: Geophysical Journal of the Royal Astronomical Society, **27**, 137–178, doi: 10.1111/j.1365-246X.1972.tb05769.

Dhemaied, A., F. Rejiba, C. Camerlynck, L. Bodet, and R. Guérin, 2011, Seismic-wave propagation modeling in viscoelastic media using the auxiliary differential equation method: Bulletin of the Seismological Society of America, **101**, 413–420, doi: 10.1785/0120100064.

Dunkin, J. W., 1965, Computation of modal solutions in layered, elastic media at high frequencies: Bulletin of the Seismological Society of America, **55**, 335–358.

Endrun, B., T. Meier, S. Lebedev, M. Bohnhoff, G. Stavrakakis, and H.-P. Harjes, 2008, S velocity structure and radial anisotropy in the Aegean region from surface wave dispersion: Geophysical Journal International, **174**, 593–616, doi: 10.1111/j.1365-246X.2008.03802.

Ezersky, M. G., L. Bodet, E. Akawwi, A. S. Al-Zoubi, C. Camerlynck, A. Dhemaied, and P.-Y. Galibert, 2013, Seismic surface-wave prospecting methods for sinkhole hazard assessment along the Dead Sea shoreline: Journal of Environmental and Engineering Geophysics, **18**, 233–253, doi: 10.2113/JEEG18.4.233.

Forbriger, T., 2003a, Inversion of shallow-seismic wavefields. I: Wavefield transformation: Geophysical Journal International, **153**, 719–734, doi: 10.1046/j.1365-246X.2003.01929.

Forbriger, T., 2003b, Inversion of shallow-seismic wavefields. II: Inferring subsurface properties from wavefield transforms: Geophysical Journal International, **153**, 735–752, doi: 10.1046/j.1365-246X.2003.01985.

Gabriels, P., R. Snieder, and G. Nolet, 1987, In situ measurements of shear-wave velocity in sediments with higher-mode Rayleigh waves: Geophysical Prospecting, **35**, 187–196, doi: 10.1111/j.1365-2478.1987.tb00812.

Godio, A., C. Strobbia, and G. De Bacco, 2006, Geophysical characterization of a rockslide in an Alpine region: Engineering Geology, **83**, 273–286, doi: 10.1016/j.enggeo.2005.06.034.

Grandjean, G., and A. Bitri, 2006, 2M-SASW: Multifold multichannel seismic inversion of local dispersion of Rayleigh waves in laterally heterogeneous subsurfaces: Application to the Super-Sauze earthflow, France: Near Surface Geophysics, **4**, 367–375.

Grelle, G., and F. M. Guadagno, 2009, Seismic refraction methodology for groundwater level determination: "Water seismic index": Journal of Applied Geophysics, **68**, 301–320, doi: 10.1016/j.jappgeo.2009.02.001.

Haines, S. S., 2007, A hammer-impact, aluminium, shear-wave seismic source: Technical Report OF 07-1406, United States Geological Survey.

Haney, M. M., and H. Douma, 2012, Rayleigh-wave tomography at Coronation Field, Canada: The topography effect: The Leading Edge, **31**, 54–61, doi: 10.1190/1.3679328.

Haskell, N. A., 1953, The dispersion of surface waves on multilayered media: Bulletin of the Seismological Society of America, **43**, 17–34.
Hayashi, K., and H. Suzuki, 2004, CMP cross-correlation analysis of multichannel surface-wave data: Exploration Geophysics, **35**, 7–13, doi: 10.1071/EG04007.
Herrmann, R. B., 2013, Computer programs in seismology: An evolving tool for instruction and research: Seismological Research Letters, **84**, 1081–1088, doi: 10.1785/0220110096.
Hibert, C., G. Grandjean, A. Bitri, J. Travelletti, and J.-P. Malet, 2012, Characterizing landslides through geophysical data fusion: Example of the La Valette landslide (France): Engineering Geology, **128**, 23–29, doi: 10.1016/j.enggeo.2011.05.001.
Hurwitz, S., R. N. Harris, C. A. Werner, and F. Murphy, 2012, Heat flow in vapor dominated areas of the Yellowstone Plateau Volcanic Field: Implications for the thermal budget of the Yellowstone Caldera: Journal of Geophysical Research: Solid Earth, **117**, B10207, doi: 10.1029/2012JB009463.
Ikeda, T., T. Tsuji, and T. Matsuoka, 2013, Window-controlled CMP cross-correlation analysis for surface waves in laterally heterogeneous media: Geophysics, **78**, no. 6, EN95–EN105, doi: 10.1190/geo2013-0010.1.
Jongmans, D., 1992, The application of seismic methods for dynamic characterization of soils in earthquake engineering: Bulletin of the International Association of Engineering Geology, **46**, 63–69, doi: 10.1007/BF02595035.
Jongmans, D., G. Bièvre, F. Renalier, S. Schwartz, N. Beaurez, and Y. Orengo, 2009, Geophysical investigation of a large landslide in glaciolacustrine clays in the Trièves area (French Alps): Engineering Geology, **109**, 45–56, doi: 10.1016/j.enggeo.2008.10.005.
Jongmans, D., and D. Demanet, 1993, The importance of surface waves in vibration study and the use of Rayleigh waves for estimating the dynamic characteristics of soils: Engineering Geology, **34**, 105–113, doi: 10.1016/0013-7952(93)90046-F.
Kennett, B. L. N., 1974, Reflections, rays, and reverberations: Bulletin of the Seismological Society of America, **64**, 1685–1696.
Konstantaki, L. A., S. F. A. Carpentier, F. Garofalo, P. Bergamo, and L. V. Socco, 2013, Determining hydrological and soil mechanical parameters from multichannel surface-wave analysis across the Alpine Fault at Inchbonnie, New Zealand: Near Surface Geophysics, **11**, 435–448, doi: 10.3997/1873-0604.2013019.
Lai, C. G., and G. J. Rix, 1998, Simultaneous inversion of Rayleigh phase velocity and attenuation for near-surface site characterization: Technical Report GIT-CEE/GEO-98-2, Georgia Institute of Technology.
Lai, C. G., G. J. Rix, S. Foti, and V. Roma, 2002, Simultaneous measurement and inversion of surface wave dispersion and attenuation curves: Soil Dynamics and Earthquake Engineering, **22**, 923–930, doi: 10.1016/S0267-7261(02)00116-1.
Lomax, A., and R. Snieder, 1994, Finding sets of acceptable solutions with a genetic algorithm with application to surface wave group dispersion in Europe: Geophysical Research Letters, **21**, 2617–2620, doi: 10.1029/94GL02635.
Martin, R., and D. Komatitsch, 2009, An unsplit convolutional perfectly matched layer technique improved at grazing incidence for the viscoelastic wave equation: Geophysical Journal International, **179**, 333–344, doi: 10.1111/j.1365-246X.2009.04278.
Martínez, M. D., X. Lana, J. Olarte, J. Badal, and J. A. Canas, 2000, Inversion of Rayleigh wave phase and group velocities by simulated annealing: Physics of the Earth and Planetary Interiors, **122**, 3–17, doi: 10.1016/S0031-9201(00)00183-7.
McMechan, G. A., and M. J. Yedlin, 1981, Analysis of dispersive waves by wave field transformation: Geophysics, **46**, 869–874, doi: 10.1190/1.1441225.
Miller, R. D., J. Xia, C. B. Park, and J. Ivanov, 1999, Multichannel analysis of surface waves to map bedrock: The Leading Edge, **18**, 1392–1396, doi: 10.1190/1.1438226.
Mokhtar, T. A., R. B. Herrmann, and D. R. Russell, 1988, Seismic velocity and Q model for the shallow structure of the Arabian Shield from short-period Rayleigh waves: Geophysics, **53**, 1379–1387, doi: 10.1190/1.1442417.
Mosegaard, K., and A. Tarantola, 1995, Monte Carlo sampling of solutions to inverse problems: Journal of Geophysical Research: Solid Earth, **100**, 12431–12447, doi: 10.1029/94JB03097.
Mota, R., and F. A. Monteiro Santos, 2010, 2D sections of porosity and water saturation from integrated resistivity and seismic surveys: Near Surface Geophysics, **8**, 575–584, doi: 10.3997/1873-0604.2010042.
Nagai, K., A. O'Neill, Y. Sanada, and Y. Ashida, 2005, Genetic algorithm inversion of Rayleigh wave dispersion from CMPCC gathers over a shallow fault model: Journal of Environmental and Engineering Geophysics, **10**, 275–286, doi: 10.2113/JEEG10.3.275.
Neducza, B., 2007, Stacking of surface waves: Geophysics, **72**, no. 2, V51–V58, doi: 10.1190/1.2431635.
Olona, J., J. Pulgar, G. Fernández-Viejo, C. López-Fernández, and J. González-Cortina, 2010, Weathering variations in a granitic massif and related geotechnical properties through seismic and electrical resistivity methods: Near Surface Geophysics, **8**, 585–599, doi: 10.3997/1873-0604.2010043.
O'Neill, A., 2003, Full-waveform reflectivity for modeling, inversion and appraisal of seismic surface wave dispersion in shallow site investigations: Ph.D. thesis, University of Western Australia.
O'Neill, A., M. Dentith, and R. List, 2003, Full-waveform P-SV reflectivity inversion of surface waves for shallow engineering applications: Exploration Geophysics, **34**, 158–173, doi: 10.1071/EG03158.
O'Neill, A., and T. Matsuoka, 2005, Dominant higher surface-wave modes and possible inversion pitfalls: Journal of Environmental and Engineering Geophysics, **10**, 185–201, doi: 10.2113/JEEG10.2.185.
OpenTopography, 2017, OpenTopography, High-Resolution Topography Data and Tools, http://www.opentopography.org, accessed 10 August 2017.
Othman, A. A. A., 2005, Construed geotechnical characteristics of foundation beds by seismic measurements: Journal of Geophysics and Engineering, **2**, 126–138, doi: 10.1088/1742-2132/2/2/007.
Park, C. B., R. D. Miller, and J. Xia, 1999, Multichannel analysis of surface waves: Geophysics, **64**, 800–808, doi: 10.1190/1.1444590.
Parsekian, A. D., K. Singha, B. J. Minsley, W. S. Holbrook, and L. Slater, 2015, Multiscale geophysical imaging of the critical zone: Reviews of Geophysics, **53**, 1–26, doi: 10.1002/2014RG000465.
Pasquet, S., 2017, SWIP releases, https://github.com/SWIPdev/SWIP/releases, accessed 10 August 2017.
Pasquet, S., L. Bodet, P. Bergamo, R. Guérin, R. Martin, R. Mourgues, and V. Tournat, 2016a, Small-scale seismic monitoring of varying water levels in granular media: Vadose Zone Journal, **15**, doi: 10.2136/vzj2015.11.0142.
Pasquet, S., L. Bodet, A. Dhemaied, A. Mouhri, Q. Vitale, F. Rejiba, N. Flipo, and R. Guérin, 2015a, Detecting different water table levels in a shallow aquifer with combined P-, surface and SH-wave surveys: Insights from V_P/V_S or Poisson's ratios: Journal of Applied Geophysics, **113**, 38–50, doi: 10.1016/j.jappgeo.2014.12.005.
Pasquet, S., L. Bodet, L. Longuevergne, A. Dhemaied, C. Camerlynck, F. Rejiba, and R. Guérin, 2015b, 2D characterization of near-surface V_P/V_S: Surface-wave dispersion inversion versus refraction tomography: Near Surface Geophysics, **13**, 315–331, doi: 10.3997/1873-0604.2015028.
Pasquet, S., L. Bodet, L. Longuevergne, A. Dhemaied, F. Rejiba, C. Camerlynck, and R. Guérin, 2012, Surface-wave dispersion stacking on a granite-micaschists contact at Plœmeur hydrological observatory, France: Presented at the Near Surface Geoscience 2012 — 18th European Meeting of Environmental and Engineering Geophysics, EAGE.
Pasquet, S., W. S. Holbrook, B. J. Carr, and K. W. W. Sims, 2016b, Geophysical imaging of shallow degassing in a Yellowstone hydrothermal system: Geophysical Research Letters, **43**, 12027–12035, doi: 10.1002/2016GL071306.
Pasquet, S., G. Sauvin, M. R. Andriamboavonjy, L. Bodet, I. Lecomte, and R. Guérin, 2014, Surface-wave dispersion inversion versus SH-wave refraction tomography in saturated and poorly dispersive quick clays: Presented at the Near Surface Geoscience 2014 — 20th European Meeting of Environmental and Engineering Geophysics, EAGE.
Pérez Solano, C. A. P., D. Donno, and H. Chauris, 2014, Alternative waveform inversion for surface wave analysis in 2-D media: Geophysical Journal International, **198**, 1359–1372, doi: 10.1093/gji/ggu211.
Raptakis, D., F. J. Chávez-García, K. Makra, and K. Pitilakis, 2000, Site effects at Euroseistest. I: Determination of the valley structure and confrontation of observations with 1D analysis: Soil Dynamics and Earthquake Engineering, **19**, 1–22, doi: 10.1016/S0267-7261(99)00025-1.
Renalier, F., D. Jongmans, A. Savvaidis, M. Wathelet, B. Endrun, and C. Cornou, 2010, Influence of parameterization on inversion of surface wave dispersion curves and definition of an inversion strategy for sites with a strong contrast: Geophysics, **75**, no. 6, B197–B209, doi: 10.1190/1.3506556.
Rix, G. J., C. G. Lai, and S. Foti, 2001, Simultaneous measurement of surface wave dispersion and attenuation curves: Geotechnical Testing Journal, **24**, 350–358, doi: 10.1520/GTJ11132J.
Rix, G. J., and E. A. Leipski, 1991, Accuracy and resolution of surface wave inversion: Recent advances in instrumentation, data acquisition and testing in soil dynamics: ASCE, 17–32.
Russel, D. R., 1987, Multi-channel processing of dispersed surface waves: Ph.D. thesis, Saint Louis University.
Sambridge, M., 1999a, Geophysical inversion with a neighbourhood algorithm. I: Searching a parameter space: Geophysical Journal International, **138**, 479–494, doi: 10.1046/j.1365-246X.1999.00876.
Sambridge, M., 1999b, Geophysical inversion with a neighbourhood algorithm. II: Appraising the ensemble: Geophysical Journal International, **138**, 727–746, doi: 10.1046/j.1365-246x.1999.00900.
Sambridge, M., 2001, Finding acceptable models in nonlinear inverse problems using a neighbourhood algorithm: Inverse Problems, **17**, 387–403, doi: 10.1088/0266-5611/17/3/302.
Sambridge, M., and K. Mosegaard, 2002, Monte Carlo methods in geophysical inverse problems: Reviews of Geophysics, **40**, 1009, doi: 10.1029/2000RG000089.

Sambuelli, L., G. P. Deidda, G. Albis, E. Giorcelli, and G. Tristano, 2001, Comparison of standard horizontal geophones and newly designed horizontal detectors: Geophysics, **66**, 1827–1837, doi: 10.1190/1.1487125.
Schmelzbach, C., D. Sollberger, S. A. Greenhalgh, H. Horstmeyer, H. Maurer, and J. O. A. Robertsson, 2016, 9C seismic data acquisition for near-surface applications: Recording, waveform reciprocity and 4C rotation: 78th Annual International Conference and Exhibition, EAGE, Extended Abstracts, WS04 B03.
Sheriff, R. E., and L. P. Geldart, 1995, Exploration seismology: Cambridge University Press.
Socco, L. V., and D. Boiero, 2008, Improved Monte Carlo inversion of surface wave data: Geophysical Prospecting, **56**, 357–371, doi: 10.1111/j.1365-2478.2007.00678.
Socco, L. V., D. Boiero, S. Foti, and R. Wisén, 2009, Laterally constrained inversion of ground roll from seismic reflection records: Geophysics, **74**, no. 6, G35–G45, doi: 10.1190/1.3223636.
Socco, L. V., S. Foti, and D. Boiero, 2010a, Surface-wave analysis for building near-surface velocity models — Established approaches and new perspectives: Geophysics, **75**, no. 5, 75A83–75A102, doi: 10.1190/1.3479491.
Socco, L. V., D. Jongmans, D. Boiero, S. Stocco, M. Maraschini, K. Tokeshi, and D. Hantz, 2010b, Geophysical investigation of the Sandalp rock avalanche deposits: Journal of Applied Geophysics, **70**, 277–291, doi: 10.1016/j.jappgeo.2009.12.005.
Socco, L. V., and C. Strobbia, 2004, Surface-wave method for near-surface characterization: A tutorial: Near Surface Geophysics, **2**, 165–185.
Sollberger, D., C. Schmelzbach, C. Van Renterghem, J. Robertsson, and S. Greenhalgh, 2016, Single-component elastic wavefield separation at the free surface using source- and receiver-side gradients: 86th Annual International Meeting, SEG, Expanded Abstracts, 2268–2273.
Song, X., H. Gu, L. Tang, S. Zhao, X. Zhang, L. Li, and J. Huang, 2015, Application of artificial bee colony algorithm on surface wave data: Computers & Geosciences, **83**, 219–230, doi: 10.1016/j.cageo.2015.07.010.
Song, X., L. Tang, X. Lv, H. Fang, and H. Gu, 2012, Shuffled complex evolution approach for effective and efficient surface wave analysis: Computers & Geosciences, **42**, 7–17, doi: 10.1016/j.cageo.2012.02.015.
St. Clair, J., 2015, Geophysical investigations of underplating at the Middle American Trench, weathering in the critical zone, and snow water equivalent in seasonal snow: Ph.D. thesis, University of Wyoming.
St. Clair, J., S. Moon, W. S. Holbrook, J. T. Perron, C. S. Riebe, S. J. Martel, B. Carr, C. Harman, K. Singha, and D. d. Richter, 2015, Geophysical imaging reveals topographic stress control of bedrock weathering: Science, **350**, 534–538, doi: 10.1126/science.aab2210.
Stockwell, J., 2017, CWP/SU: Seismic Unix, http://www.cwp.mines.edu/cwpcodes, accessed 10 August 2017.
Strobbia, C., and S. Foti, 2006, Multi-offset phase analysis of surface wave data (MOPA): Journal of Applied Geophysics, **59**, 300–313, doi: 10.1016/j.jappgeo.2005.10.009.
Strobbia, C., A. Laake, P. Vermeer, and A. Glushchenko, 2011, Surface waves: Use them then lose them. Surface-wave analysis, inversion and attenuation in land reflection seismic surveying: Near Surface Geophysics, **9**, 503–514, doi: 10.3997/1873-0604.2011022.
Thomson, W. T., 1950, Transmission of elastic waves through a stratified solid medium: Journal of Applied Physics, **21**, 89–93, doi: 10.1063/1.1699629.
Turesson, A., 2007, A comparison of methods for the analysis of compressional, shear, and surface wave seismic data, and determination of the shear modulus: Journal of Applied Geophysics, **61**, 83–91, doi: 10.1016/j.jappgeo.2006.04.005.
Uhlemann, S., S. Hagedorn, B. Dashwood, H. Maurer, D. Gunn, T. Dijkstra, and J. Chambers, 2016, Landslide characterization using P- and S-wave seismic refraction tomography — The importance of elastic moduli: Journal of Applied Geophysics, **134**, 64–76, doi: 10.1016/j.jappgeo.2016.08.014.
Uyank, O., 2011, The porosity of saturated shallow sediments from seismic compressional and shear wave velocities: Journal of Applied Geophysics, **73**, 16–24, doi: 10.1016/j.jappgeo.2010.11.001.
Wathelet, M., 2008, An improved neighborhood algorithm: Parameter conditions and dynamic scaling: Geophysical Research Letters, **35**, L09301, doi: 10.1029/2008GL033256.
Wathelet, M., 2017, Geopsy.org packages, http://www.geopsy.org/download.php, accessed 10 August 2017.
Wathelet, M., D. Jongmans, and M. Ohrnberger, 2004, Surface-wave inversion using a direct search algorithm and its application to ambient vibration measurements: Near Surface Geophysics, **2**, 211–221, doi: 10.3997/1873-0604.2004018.
Werner, C., S. L. Brantley, and K. Boomer, 2000, CO_2 emissions related to the Yellowstone volcanic system. 2: Statistical sampling, total degassing, and transport mechanisms: Journal of Geophysical Research: Solid Earth, **105**, 10831–10846, doi: 10.1029/1999JB900331.
Xia, J., R. D. Miller, and C. B. Park, 1999, Estimation of near-surface shear-wave velocity by inversion of Rayleigh waves: Geophysics, **64**, 691–700, doi: 10.1190/1.1444578.
Xia, J., R. D. Miller, C. B. Park, and G. Tian, 2003, Inversion of high frequency surface waves with fundamental and higher modes: Journal of Applied Geophysics, **52**, 45–57, doi: 10.1016/S0926-9851(02)00239-2.
Xia, J., R. D. Miller, C. B. Park, E. Wightman, and R. Nigbor, 2002, A pitfall in shallow shear-wave refraction surveying: Journal of Applied Geophysics, **51**, 1–9, doi: 10.1016/S0926-9851(02)00197-0.
Zhang, S. X., and L. S. Chan, 2003, Possible effects of misidentified mode number on Rayleigh wave inversion: Journal of Applied Geophysics, **53**, 17–29, doi: 10.1016/S0926-9851(03)00014-4.
Zywicki, D., and G. Rix, 2005, Mitigation of near-field effects for seismic surface wave velocity estimation with cylindrical beamformers: Journal of Geotechnical and Geoenvironmental Engineering, **131**, 970–977, doi: 10.1061/(ASCE)1090-0241(2005)131:8(970).